

Reducing Co/O Band Overlap through Spin State Modulation for Stabilized High Capability of 4.6V LiCoO₂

Jicheng Zhang¹, Deniz Wong², Qinghua Zhang³, Nian Zhang⁴, Christian Schulz², Maciej Bartkowiak², Ke An⁵, Lin Gu³, Zhongbo Hu¹, Xiangfeng Liu^{1,6*}

1 Center of Materials Science and Optoelectronics Engineering, College of Materials Science and Optoelectronic Technology, University of Chinese Academy of Sciences, Beijing 100049, P. R. China.

2 Helmholtz-Zentrum Berlin für Materialien und Energie, Hahn-Meitner-Platz 1, D-14109 Berlin, Germany.

3 Beijing National Laboratory for Condensed Matter Physics, Institute of Physics, Chinese Academy of Science, Beijing 100190, P. R. China.

4 Shanghai Institute of Microsystem and Information Technology, Chinese Academy of Sciences, Shanghai 200050, P. R. China.

5 Neutron Scattering Division, Oak Ridge National Laboratory, Oak Ridge, Tennessee 37830, United States.

6 CAS Center for Excellence in Topological Quantum Computation, University of Chinese Academy of Sciences, Beijing 100190, China.

ABSTRACT: High-voltage LiCoO₂ (LCO) attracts great interest because of large specific capacity but suffers from oxygen release, structural degradation, and quick capacity drop. These daunting issues root from the inferior thermodynamics and kinetics of the triggered oxygen anion redox (OAR) at high voltages. Herein, a tuned redox mechanism with almost only Co redox is demonstrated by an atomically engineered high spin LCO. The high spin Co network reduces the Co/O band overlap, eliminates the adverse phase transition of O₃→H1-3, delays the exceeding of O 2p band over the Fermi level and the resulted excessive O→Co charge transfer at high voltages. This function intrinsically promotes the Co redox and restrains the O redox, fundamentally addressing the issues of O₂ release and coupled detrimental Co reduction. Moreover, the chemo-mechanical heterogeneity caused by different kinetics of Co/O redox centers and the inferior rate performance limited by slow O redox kinetics are simultaneously improved owing to the suppression of slow OAR and the excitation of fast Co redox. The modulated LCO delivers an ultra-high rate capacity of 216 mAh g⁻¹ (1C) and 195 mAh g⁻¹ (5C), as well as a high capacity retention of 90.4% (@100 cycles) and 86.9% (@500 cycles). This work sheds new light to the design for a wide range of O redox cathodes.

INTRODUCTION

LiCoO₂ (LCO) cathode is ideal for 3C electronics due to a high electronic conductivity (10^{-8} – 10^{-7} s cm⁻¹) and tap density (>4.2 g cm⁻³).¹ With a typical O3 structure, LCO forms Co³⁺ with a low spin state configuration ($t_{2g}^6 e_g^0$).² In LCO with such characteristics, only half of the Co³⁺ could be reversibly oxidized to Co⁴⁺. With oxidizing more than 50% Co³⁺ to Co⁴⁺, O anion redox (OAR) is ubiquitously triggered.^{3,4} Although the OAR elevates the overall capacity of LCO, severe structural degradation and sharp capacity decay are inevitably aroused.⁵⁻⁸ These problems originate from the intrinsic OAR issues on thermodynamics and kinetics. First of all, OAR shows inferior thermodynamics. Because of the poor stability of the oxidized O species and the susceptible O→Co charge transfer process, the over-oxidation of lattice O²⁻ to O₂ and over-reduction of Co⁴⁺ to detrimental reduced Co cations are reported.⁹ Secondly, the significant differences in Co/O redox kinetics would cause chemo-mechanical heterogeneity, which is verified by the detected uneven chemical states in Co and O and phase generation of hybrid H1-3 in researches.^{10,11} These are the pivotal obstacles that limit the practical applications of high-voltage (especially 4.6V) LCO. Although improvements have been made on high-

voltage LCO through surface coating and bulk doping,¹²⁻²¹ the practical performances are still far from satisfactory. The intrinsic OAR issues remain to be resolved. Moreover, these strategies inevitably introduce excessive inert elements, which compromises the delivered capacity. For example, our group recently reported a Mg/F doped LCO, which reduces the delivered capacity from about 180 to only about 170 mAh g⁻¹ with a 4.5V ceiling.¹⁵

A fundamental solution for addressing the thermodynamic instability and slow kinetics of OAR in high-voltage LCO lays on inhibiting or even eliminating OAR and simultaneously deepening Co redox. However, this is difficult to achieve. The generation of OAR in LCO is determined by its intrinsic electronic structure with a high Co-O covalency.²² The key to the redox mechanism of LCO is which energy band does the Fermi level sit on. Specifically, the Co^{3+/4+} occurs when the Fermi level locates at the t_{2g} band, while the OAR occurs when the Fermi level is on the overlapped O/Co band.²² For eliminating or delaying the triggering of OAR at high voltages, it is necessary to fundamentally regulate the evolution of band structure for LCO. This requires a comprehensive regulation of

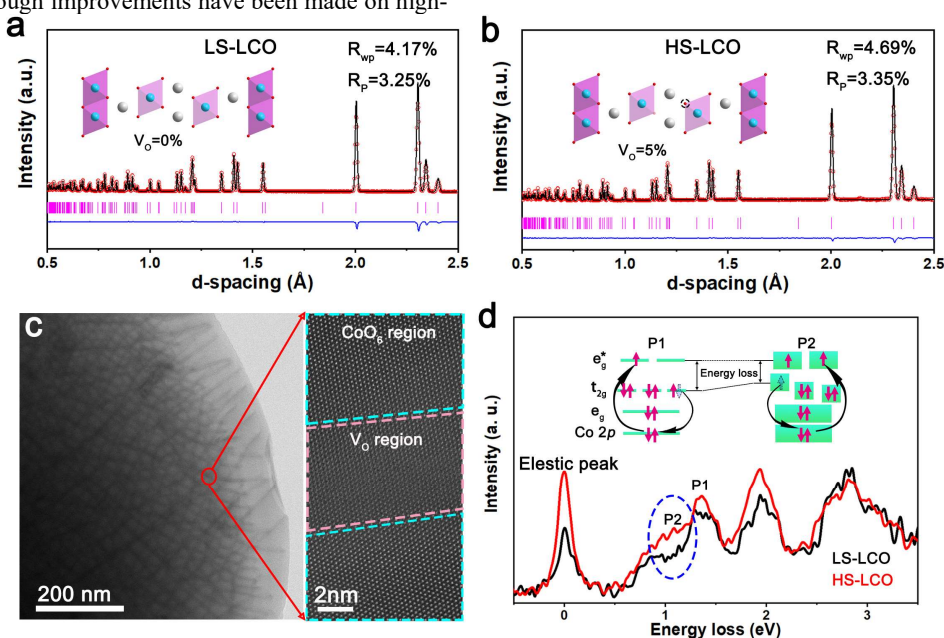


Figure 1. a, b) Rietveld refined neutron diffraction patterns of LS-LCO (a) and HS-LCO (b). c) AC-STEM images of HS-LCO. d) Co L-edge RIXS spectra. The insets declare the corresponding RIXS process.

structural features in LCO those are correlated to the OAR chemistry. Although abundant structural strategies have been proposed, up to now, the elimination of OAR in high-voltage LCO has still not been reported yet.

According to classical crystal field theory, the band structure of LCO is directly related to the local Co-O coordination. The recent researches related to this point have been published.^{5,23} For example, one work reported that the curvature of the CoO₂ is critical for O₂ generation.⁵ Pan et al. discovered that the lattice strain and mismatch are the basic causes of the unstable lattice oxygen reaction and lattice oxygen escape.²³ In addition, some works have also explored the redox chemistry of lattice oxygen in LCO.^{24,25} For example, Yang et al. discovered a reduced distance of the intralayer O–O in LCO lattice with charge.²⁴ However, the correlation of lattice oxygen redox chemistry and the

structural characteristics are still not clear. In this backdrop, the exploration of new strategies with a fundamental structural aspect, for addressing the intrinsic OAR issues of inferior thermodynamics and kinetics and realizing the high performances in capacity, stability and rate capability of 4.6V LCO, is urgent and important.

In this work, a tuned redox mechanism with almost only Co redox is demonstrated by an atomically engineered high spin LCO. A nanoribboned network structure rich with high spin Co is formed. The high spin Co network eliminates the adverse phase transition of O3→H1-3, delays the exceeding of O 2p band over the Fermi level and the resulted excessive O→Co charge transfer at high voltages. This largely elevates the threshold voltage for triggering OAR from 4.2 V to over 4.5 V, restricting the O redox in 4.6 V LCO within a very low degree

and reversible form of $O^{2-} \leftrightarrow O^{\cdot}$. It intrinsically promotes the Co redox and restrains the O redox, fundamentally addressing the issues of O_2 release and coupled detrimental Co reduction. Moreover, the chemo-mechanical heterogeneity caused by different kinetics of Co/O redox centers and the inferior rate performance limited by slow O redox kinetics are simultaneously improved owing to the suppression of slow OAR and the excitation of fast Co redox. A comprehensive and remarkable improvement in capacity, cycling stability, and rate capability is obtained. High spin LCO delivers high capacity of about 216 mAh g^{-1} (@1C), 195 mAh g^{-1} (@5C) and superior cycling retentions of 86.9% (@500 cycles@5C). This novel spin state modulation strategy and the proposed insights would shed new light to the design for a wide range of O redox cathodes.

RESULTS AND DISCUSSION

Tuning the spin state of Co. Here the spin state of Co is modulated through inducing interfacial lattice mismatch stress. A novel grain fusion method is developed here, as illustrated by Figure S1. In order to ensure sufficient interfaces for fusion and maintain the interfacial lattice mismatch stress during the synthesis, a nanoscale cobalt oxalate precursor and a trace amount of additive are used. The material synthesized in this way is the high spin LCO, which is labeled as HS-LCO. For comparisons, the samples are prepared with micron and nano precursors without additives, which are labeled as low spin LCO (LS-LCO) and HS-LCO with no additives (HS-LCO-NO), respectively. The structures and morphologies of nano and micro precursors are shown in Figure S2. And the morphologies for the synthesized samples are provided in Figure S3. Compared with the large grain morphology of LS-LCO, the particle of HS-LCO is integrated by many small grains. Interestingly, the morphologies of HS-LCO-NO and LS-LCO are similar.

X-ray diffraction (XRD) profiles (Figure S4) show that LS-LCO, HS-LCO-NO and HS-LCO are in accordance with the crystal group of R-3m. XRD Rietveld refinements declare some differences in cell parameters (Figure S5, Table S1). Compared with LS-LCO, HS-LCO and HS-LCO-NO declares a somewhat defected structure, which is evidenced by the lower peak intensity ratio of 003/104 for LS-LCO than HS-LCO and HS-LCO-NO.^{26,27} More specific structural details are interpreted by neutron diffraction (ND) Rietveld refinements (Figure 1a, 1b, Table S2 and S3). In HS-LCO, 5 % oxygen vacancies are discovered, which is verified by X-ray photoelectron spectroscopy (XPS, Figure S6) as well. Previous studies have shown that the presence of O defects elevate the spin states of Co from low ($t_{2g}^6 e_g^0$) to high ($t_{2g}^5 e_g^1$) in LCO.²⁸

Spherical aberration-corrected scanning transmission electron microscopy (AC-STEM) image manifests that abundant nanoribbons are found to form a network structure in HS-LCO (Figure 1c) but not in HS-LCO-NO (Figure S7). These nanoribbons are formed by interfacial fusion, which is rich in defects. Compared with the atomic arrangement outside the nanoribbons, the atomic array in the nanoribbons is a little disordered. The line intensity profile across the nanoribbon indicates a contractive lattice (Figure S8), which would influence the spin state.²⁹ Figure S9 reflects the images for specific arrangement of Co cations in regions near and far away from the nanoribbons in HS-LCO, respectively, where the distances between the adjacent Co columns and the angles between the column alignments are different. It indicates that the fusion interface affects the arrangement of atoms around it. The lattice stress field is

thus developed. Under normal conditions, defects will be removed after annealing.³⁰ Here the trace additive promotes and stabilizes the defects. The distributions of added elements in HS-LCO are not uniform, which is demonstrated by the X-ray photoelectron spectroscopy (XPS) in Figure S10.

Electron paramagnetic resonance (EPR) tested at room temperature demonstrates the high spin state of Co in HS-LCO by detecting abundant single electrons (Figure S11). The EPR linewidth is widened for HS-LCO than LS-LCO. This could be explained by the spin-spin intercalation between the high spin Co cations. ⁷Li magic-angle spinning (MAS) nuclear magnetic resonance (NMR) in Figure S12 indicates that, in addition to the 0 ppm peak, HS-LCO has extra signals at 4.4, -5.3 ppm and -15.6 ppm, which is yielded by oxygen defect and high spin Co.³¹ Based on the peak ratio, the content of high spin Co in HS-LCO is calculated to be about 4.7%. The Co L edge resonant inelastic X-ray scattering (RIXS) spectra (excitation energy of 780.7 eV) is conducted on LS-LCO and HS-LCO (Figure 1d). A P2 signal appears at the lower energy loss of P1 in the spectra for HS-LCO. The inset interprets the RIXS process of these peaks. It further proves the higher spin state of Co in HS-LCO than LS-LCO. The magnetic measurements of both samples are conducted (Figure S13). The molar magnetic susceptibility is much higher for HS-LCO than LS-LCO, which further verifies the existence of high spin state of Co in HS-LCO.

Electrochemical characterizations. Differences are shown in the cyclic voltammetry (CV) plots for HS-LCO and LS-LCO (Figure 2a). In contrast to LS-LCO, HS-LCO has a lower inflection voltage of oxidation peak for $O3/O3'$ transition as the arrow indicated. This is from the withdrawal of electrons in higher energy occupied states for HS-LCO than LS-LCO. In addition, a sharp redox peak shape is demonstrated by HS-LCO, reflecting a better redox kinetics. Increasing the current density from 1 C to 5 C, the better-maintained charge-discharge curve and the higher capacity maintenance for HS-LCO than LS-LCO verify the quick kinetics of HS-LCO (Figure 2b). The Li^+ diffusion coefficient (D_{Li}) for the charging process calculated from galvanostatic intermittent titration technique (GITT) manifests a better Li^+ transportation kinetics in HS-LCO (Figure S14). The higher D_{Li} of HS-LCO than LS-LCO at low state of charge (SoC) verifies the high spin Co of HS-LCO. And at high SoC, the D_{Li} is largely reduced for LS-LCO but not for HS-LCO. This supports the inhibition of O redox in HS-LCO.³² The in situ electrochemical impedance spectroscopy (EIS) displays different impedance evolutions of LS-LCO and HS-LCO upon charging (Figure S15). Compared with LS-LCO, HS-LCO maintains smaller impedances. From the shape change of EIS curves, a simpler redox behavior for HS-LCO than LS-LCO is conveyed.

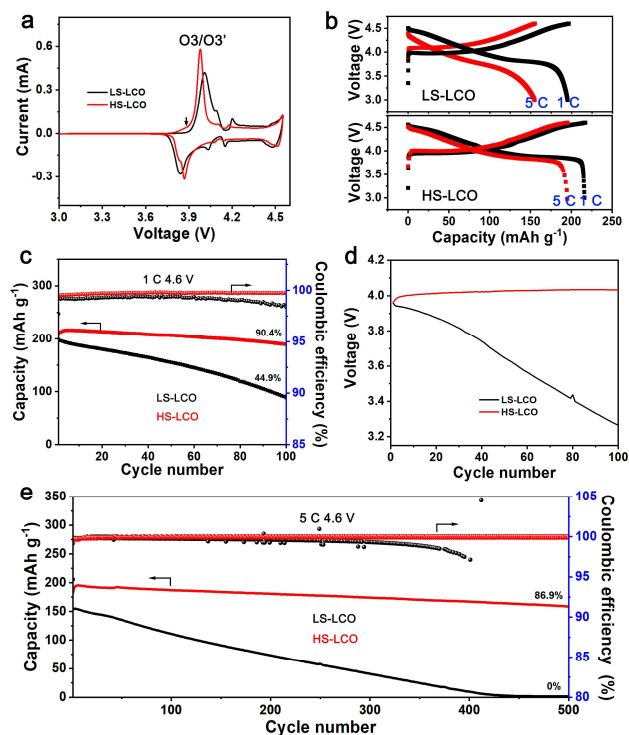


Figure 2. a) Cyclic voltammety plots. b) The charge-discharge profiles of LS-LCO and HS-LCO. c) The cycling performances at 1 C

of cathodes with a 4.6V voltage ceiling. d) The average discharge voltage versus cycle number at 1C. e) The cycling performances at 5 C of cathodes with a 4.6V voltage ceiling. 1 C is set as 200 mA g⁻¹.

With a 4.6 V voltage ceiling, the delivered capacity at 1 C for LS-LCO is only 198 mAh g⁻¹, while that for HS-LCO is raised to 216 mAh g⁻¹ (Figure 2c). Remarkably, after 100 cycles, the capacity retentions of LS-LCO and HS-LCO are 44.9% and 90.4%, respectively. The higher Coulomb efficiency for HS-LCO than LS-LCO demonstrates that the redox reactions in HS-LCO is more reversible, which correlates to the modulated redox mechanism. Figure 2d suggests a maintained voltage for HS-LCO but a seriously voltage decay for LS-LCO. This confirms that HS-LCO inhibits the lattice oxygen escape well. Moreover, when cycling at 5 C, the improvements of HS-LCO is more obvious (Figure 2e). Compared with LS-LCO (~150 mAh g⁻¹), HS-LCO delivers a much higher capacity (~195 mAh g⁻¹). After 500 cycles, the capacity retention for HS-LCO (86.9%) is much increased compared with that for LS-LCO (0%). The improvements for the 4.5V condition are also obvious (Figure S16 and S17). The delivered capacity is elevated from 181 mAh g⁻¹ for LS-LCO to 190 mAh g⁻¹ for HS-LCO. XRD plots of electrodes before and after cycling declare an improved structural stability of HS-LCO (Figure S18). The electrochemical behaviors of HS-LCO, LS-LCO and HS-LCO-NO are compared through the (dis)charge curves (Figure S19).

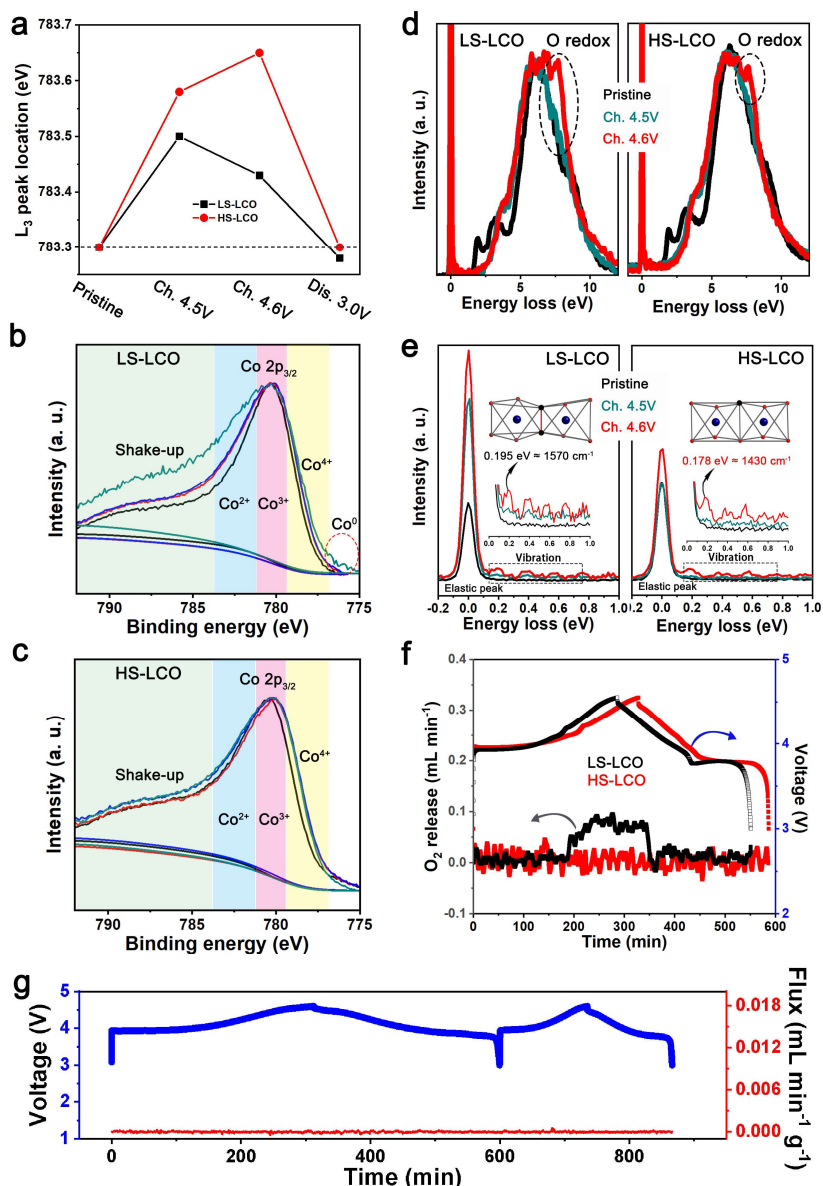


Figure 3. a) The L₃ peak locations in Co L-edge XAS spectra for electrodes at different states of charge. b, c) The Co 2p XPS spectra for LS-LCO electrodes (b) and HS-LCO electrodes (c). d) Normalized O-K edge RIXS spectra for electrodes at different states of charge. e) The enlarged elastic and O–O vibration peaks in the RIXS spectra. The insets depict the structural characteristics of oxidized oxygen in lattice. f, g) Operando DEMS of O₂ evolution for LS-LCO and HS-LCO with a 4.55V ceiling (f) and for HS-LCO with a 4.6V ceiling (g).

It demonstrates the function of high spin state of Co in stabilizing electrochemical performances. The comparison of the electrochemical performances between HS-LCO and other reported modified materials is listed in Table S4. X-ray emission spectrum demonstrate that, after a long cycling, the high spin state of Co in HS-LCO is well retained (Figure S20).

Redox mechanisms. Combined with various techniques, the redox behaviors of Co and O in LS-LCO and HS-LCO are proved to be different. Compared with LS-LCO, a deeper Co redox is exhibited in HS-LCO. As shown in Figure S21, Co L₃-edge soft X-ray absorption spectra (XAS) spectra in total fluorescence yield (TFY) mode for charged samples is composed of peak α and β , which are generated by electron jumps from Co 2p state to e_g^* band and t_{2g} band, respectively.³³ The XAS processes for the signals are depicted in Figure S22. Compared

with LS-LCO, the β signal for HS-LCO shift to higher energy, indicating an enlarged range for t_{2g} band. In addition, as illustrated by the areas for β signals, more Co⁴⁺ cations are yielded in HS-LCO than LS-LCO with charge.

The Co L₃ peak positions plotted in Figure 3a show different Co charge evolutions in two materials. It is demonstrated that Co^{3+/4+} oxidation occurs less in LS-LCO than HS-LCO at a 4.5-V charged state. With further charging to 4.6V, the Co oxidation degree in LS-LCO is decreased, while which continues to deepen in HS-LCO. XPS verifies the above results (Figure 3b and 3c). With deepening the charge state, LS-LCO expresses an enhanced Co²⁺ signal. This illustrates that some abnormal electron filling into the Co energy band of LS-LCO upon charge, which may come from the O→Co charge transfer. This would be demonstrated in the following. Shake-up satellites are

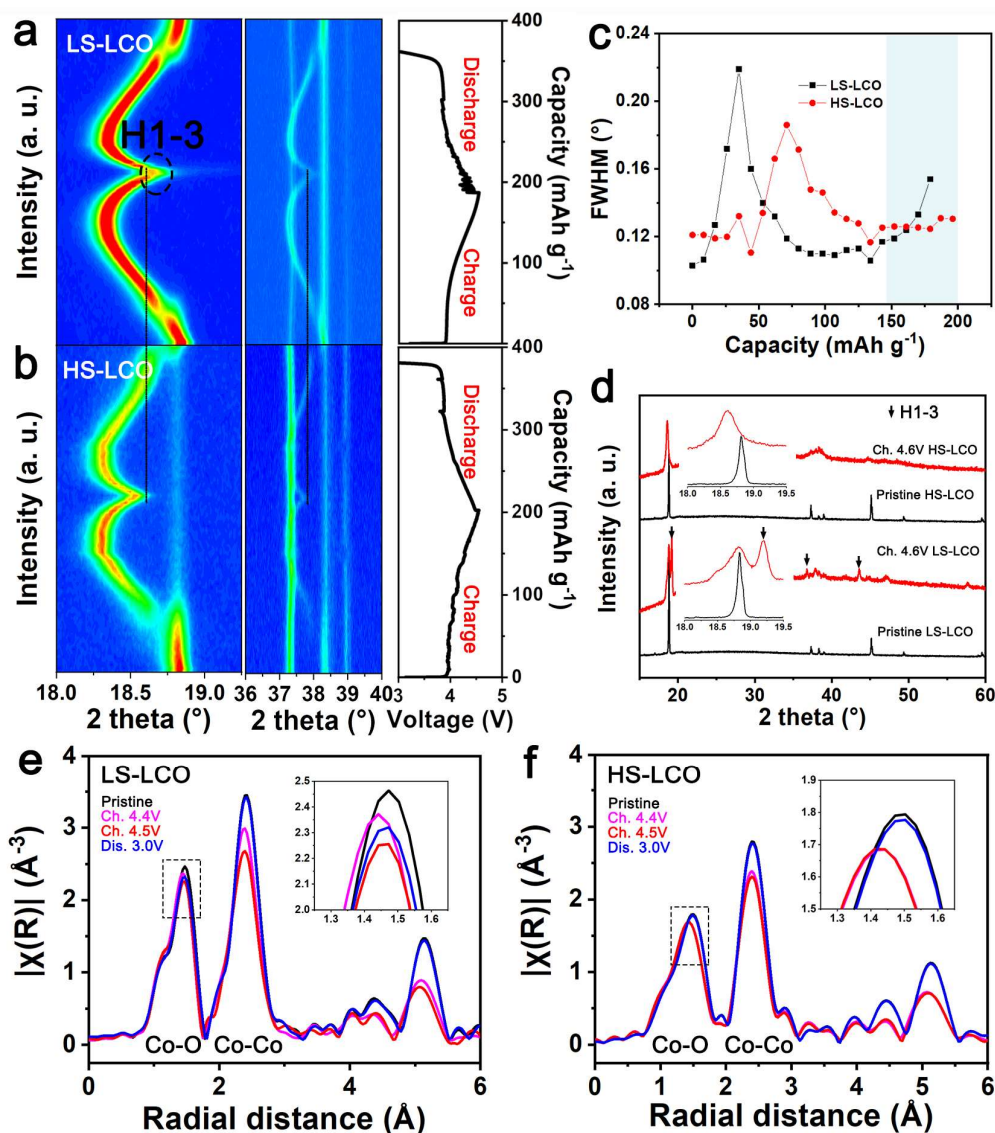


Figure 4. a, b) In situ XRD mappings of LS-LCO (a) and HS-LCO (b). c) The FWHM evolutions for 003 peaks in the in situ XRD plots. d) The ex situ XRD plots for pristine and 4.6-V charged LS-LCO and HS-LCO electrodes. e, f) Fourier transformed Co K-edge EXAFS spectra of electrodes for LS-LCO (e) and HS-LCO (f).

described as intrinsic energy losses while the photoelectron leaves the hosting atom. An intensity raise in shake-up peak is shown for LS-LCO, which manifests that the electrons on valence band are increasingly prone to jump to higher energy levels.³⁴ When LS-LCO is charged to 4.6 V, Co^{0+} signal is spotted. While these phenomena are not discovered in HS-LCO. And the redox reversibility is also largely improved for HS-LCO, as evidenced by the XPS spectra of the pristine and one-cycle charge-discharged electrodes (Figure S23).

The OAR is almost eliminated in HS-LCO. The O K-edge RIXS mapping tests are performed. The signal at about the excitation energy of 531 eV features the O redox.³⁵ With charging the electrodes to 4.55 V, the O redox featured signal is obviously detected in LS-LCO but not in HS-LCO (Figure S24). The O K-edge RIXS spectra for electrodes at different states of charge reflect the specific O properties (Figure 3d). The O redox featured peak (at about 7.5 eV) is discovered in LS-LCO but not (or almost not) in HS-LCO. The integral area of the elastic peak reflects the content of O with an electron hole (O^-).³⁶

As illustrated by the evolution for elastic peaks in Figure 4e, with charging, O^- is increasingly produced in LS-LCO but almost not in HS-LCO. The integral areas of elastic peaks for LS-LCO and HS-LCO are quantitatively provided in Figure S25. It declares the threshold voltage for OAR is elevated to over 4.5V in HS-LCO, which is consistent with above results. The low degree of OAR renders HS-LCO a better redox reversibility, as evidenced by the complete recovery of the spectra for cycled HS-LCO electrode in Figure S26.

The characteristics of the oxidized O species are revealed by the vibrated peaks, whose frequency are 0.195 and 0.178 eV for 4.6-V charged LS-LCO and 4.6-V charged HS-LCO, respectively. Because the response frequency of O_2 is 0.2 eV, it is clear that the oxidized O product in HS-LCO is further away from O_2 in nature than that in LS-LCO.³⁷ A larger O–O distance and a lower O–O interaction are manifested for HS-LCO than LS-LCO, which favors an improved bonding stability between oxidized O species and bulk lattice.

Operando differential electrochemical mass spectrometry (DEMS) detects obvious amount of O_2 in LS-LCO but not in HS-LCO with a charge voltage ceiling of 4.55V (Figure 3f). The further test for HS-LCO illustrates that cycling at 0.1 C and 0.2 C with a 4.6V ceiling, no O_2 is released from the lattice of HS-LCO, manifesting that the O_2 release is complete addressed in HS-LCO.

Restrained structural changes. The in situ XRD experiments for LS-LCO and HS-LCO are performed (Figure 4a and 4b). With charge, the $O3$ phase is transformed to $O3'$. The onset for phase transition of $O3 \rightarrow O3'$ is postponed from about 10 mAh g^{-1} for LS-LCO to 40 mAh g^{-1} for HS-LCO. A H1-3 phase is generated in LS-LCO but not in HS-LCO. An alleviative structural expansion and collapse is illustrated by Rietveld refinements of HS-LCO (Figure S27). The evolutions for full width at half maximum (FWHM) of the 003 peaks of both materials upon charge are provided in Figure 4c. Two rises in FWHM are discovered for LS-LCO at the capacity ranges of 10–70 mAh g^{-1} and 140–175 mAh g^{-1} , which correspond to $O3 \rightarrow O3'$ transition and O redox.³⁸⁻⁴⁰ While only one rise in FWHM, which is caused by the $O3 \rightarrow O3'$ transition, is discovered for HS-LCO. The FWHM lift implies increased structural complexity and distortion. Specifically, distorted CoO_6 slabs are exhibited in LS-LCO at high voltages, which is inhibited in HS-LCO. This is supported by the Rietveld refinement for ex-situ XRD, which demonstrates restrained variations in O–O distance and O–Co–O angle for HS-LCO upon delithiating (Figure S28). The Rietveld refinement results are listed in Table S5. And after prolonged battery cycling, the lattice defects, interfacial lattice mismatch, associated stress of the HS-LCO cathode could also be well maintained. By interpreting the XRD plots for pristine and long-cycled HS-LCO electrodes (Figure S29), the dislocation density (δ) and micro strain (ϵ) for pristine and cycled cathodes are calculated. After a long cycling, the values for these parameters are well retained.

The ex situ XRD plots for 4.6-V charged electrodes also present remarkable differences (Figure 4d). Charging the pristine LS-LCO electrode to 4.6 V changes part of the O framework from a $O3$ stack (ACBACB) into a hybrid H1-3 stack, which yields some lattice displacement and structural distortions.⁴¹ While the 4.6-V charged HS-LCO totally maintains the pristine $O3$ structure. This is supported by the CV results tested with a widened voltage range (Figure S30). It demonstrates that, with a deeper charge, the structure complexity is increased in LS-LCO but not in HS-LCO. Raman spectra of electrodes for LS-LCO and HS-LCO also support above data (Figure S31). Different symmetry evolutions of LS-LCO and HS-LCO are reflected by the changes of O–Co–O bending vibration (E_g) and Co–O stretching vibration ($A1g$) peaks.⁴² With charge, the symmetry of LS-LCO decreases rapidly, as evidenced by the sharp decline even disappearance of E_g and $A1g$ peaks. This has been extensively reported in other studies.⁴³ However, these two peaks still exist when HS-LCO is charged to 4.5 V, which indicates a maintained hexagonal symmetry. In addition, an improved structural reversibility is demonstrated by HS-LCO. Peak decline and Co_3O_4 signals are discovered in 3.0-V discharged LS-LCO but not in 3.0-V discharged HS-LCO.

The raw extended X-ray absorption fine structure (EXAFS) data of Co in the k-space of 0–14 \AA^{-1} are provided (Figure S32). A new peak located at about 12.5 \AA^{-1} , representing the deformed CoO_6 , is appeared for 4.5-V charged LS-LCO. While HS-LCO does not show this new peak. The Fourier-transformed (FT) k^2 -

weighted EXAFS spectra explore the coordination evolutions of Co in LS-LCO and HS-LCO at different states of charge (Figure 4e and 4f). For LS-LCO, the structural distortion is gradually increased upon delithiating, which is illustrated by the constantly intensity decays of Co–O and Co–Co shell peaks. Especially, with further charging the LS-LCO electrode from 4.4V to 4.5V, the Co–O bond length is abnormally increased, which is evidenced by the right shift of the Co–O shell peak. This comes from an Co reduction occurred at 4.5V. Moreover, after one cycle, the irreversible decrease in shell peaks have arisen for LS-LCO. While HS-LCO well restrains these phenomena. This declares that the over-reduction of Co/over-oxidation of O and the irreversible structural degeneration are well restrained for HS-LCO.

Underlying mechanism for the restrained OAR. Based on the Rietveld refined CoO_6 octahedron configurations for delithiated LS-LCO and HS-LCO in Figure S27, the theoretical calculations are conducted. As Figure 5a shows, the energy orbitals for delithiated HS-LCO are sharp and narrow, while those for delithiated LS-LCO are much broadened. This is because that the varied O–O distances and O–Co–O angles of delithiated LS-LCO and HS-LCO influence the hybrid $Co3d/O2p$ orbital configurations for octahedron. The lower O–O distance and O–Co–O angle compresses the CoO_6 octahedron of delithiated LS-LCO, which complicates the electron environment around the orbitals and widens the distribution range of energy levels. While this influence is not implemented in delithiated HS-LCO due to the changeless of the O–O distance and O–Co–O angle.

Of all the energy levels, t_{2g} and e_g deserve to be noted. The levels above t_{2g} are dominated by Co and the levels below e_g are dominated by O, which show Co character and O character, respectively.⁴⁴ The $Co^{3+/4+}$ transitions in LCO are implemented by the electron stripping and filling on t_{2g} . The broadening and shifting of the energy levels will result in a deep band overlap for Co character and O character. With charge, when the Fermi level is lower shifted to the overlapped energy band, an intense O \rightarrow Co charge transfer is yielded, which tends to induce over-oxidization of O and over-reduction of Co. Therefore, when the band overlap is restrained, OAR and unfavored O \rightarrow Co charge transfer are reduced. The Co L-edge RIXS mappings of the 4.6-V charged electrodes in Figure 5b declare that the highest electron density in t_{2g} band located higher for delithiated HS-LCO than delithiated LS-LCO, which contributes to a reduced overlap of t_{2g} and O 2p states for HS-LCO in delithiation.

Detailed experiments are conducted to prove this point. Raman spectra of 4.5-V charged electrodes for LS-LCO and HS-LCO tested at two laser powers are obtained. As Figure 5c shows, LS-LCO electrode declares no Co_3O_4 signals at a low power but obvious Co_3O_4 signals at a high powder. While no Co_3O_4 signals are discovered in HS-LCO. This result illustrates that, with high energy radiation, the unfavored O \rightarrow Co charge transfer is intense in delithiated LS-LCO but none in delithiated HS-LCO. A better thermodynamic stability of HS-LCO than LS-LCO is illustrated. In addition, the two peaks of HS-LCO at 1mW are attributed to the O–Co–O bending (E_g) and Co–O stretching ($A1g$), which illustrates an improved symmetry of the delithiated HS-LCO again.

The overcharge experiment is also conducted to reflect this point. Constant-voltage-charge is conducted on the 4.6-V charged electrodes for 12 hours (the sample is labeled as Ch. 4.6 V-12h). A much lower balanced current for HS-LCO than LS-LCO is manifested (Figure 5d), which declares that the side

reactions are much less in delithiated HS-LCO. This is further verified by the XPS (Figure 5e) results for the corresponding electrodes. Intensified bulk O₂ signal is observed in Ch. 4.6V-12h LS-LCO but not in Ch. 4.6V-12h HS-LCO.

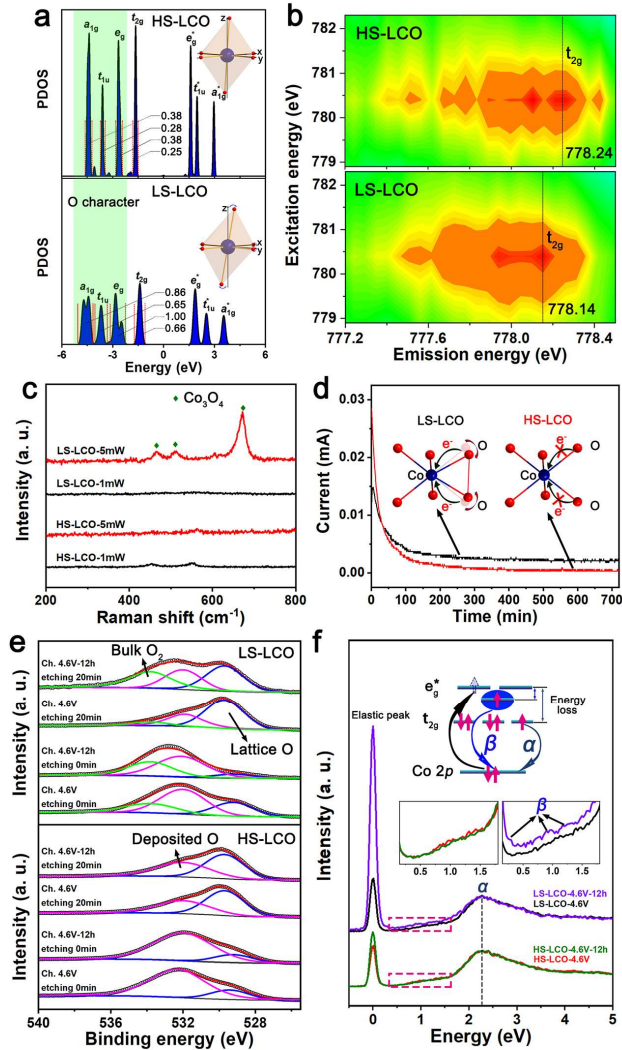


Figure 5. a) Calculated energy levels for the CoO₆ octahedrons in delithiated HS-LCO and delithiated LS-LCO, respectively. b) The Co L-edge RIXS mappings of the 4.6-V charged electrodes for HS-LCO and LS-LCO. c) The Raman spectra for 4.5-V charged electrodes at laser powers of 1 mW and 5 mW. d) The current plots for the constant-voltage-charge conducted on 4.6 V electrodes. e) The O 2p XPS spectra of the electrodes for HS-LCO and LS-LCO. f) The Co L-edge RIXS spectra for 4.6-V charged electrodes before and after constant-voltage charge.

The Co RIXS of the 4.6-V charged electrodes before and after constant-voltage-charge is also tested (Figure 5f). The electronic structure of 4.6-V charged HS-LCO barely changes after conducting constant-voltage-charge, which can be deduced by its almost identical RIXS spectra for HS-LCO-4.6V and HS-LCO-4.6V-12h. Differently, after constant-voltage charging the LS-LCO-4.6V-12h, an enhanced elastic peak and the newly

emerged inelastic peaks (β) are discovered. The increase of the elastic peak illustrates a weakened interaction between the electrons at activated and ground states in LS-LCO-4.6V-12h, which illustrates a varied electronic environment between the e_g^* and t_{2g} bands. The appeared inelastic peaks of β , correlated with the occupied electrons above the t_{2g} band, demonstrates some reduced Co cations.

These results indicate that, with external stimuli, obvious unfavorable O \rightarrow Co charge transfer occurs. While these adverse phenomena are completely suppressed in delithiated HS-LCO, indicating a very good thermodynamic stability. During the constant voltage charge, LS-LCO produces a large amount of unfavorable O \rightarrow Co charge transfer, yields O₂ and detrimental reduced Co cations. Simultaneously, the crystal structure of LS-LCO becomes more complex (Figure S33). These behaviors increase the band overlap and even cause the O 2p band to exceed the Fermi level, inducing a short but violent charge transfer. It explains the abnormal increase of current signal of LS-LCO at the early stage of constant voltage charge in Figure 5d (Figure S34 shows the amplification within 100 min). However, the structure of HS-LCO barely changes after the constant voltage charge, which confirms above results.

These results indicate that the energy band details are the key to the O \rightarrow Co charge transfer of LCO at high voltages. And the O \rightarrow Co charge transfer requires the Fermi level to pass through the overlapping of O and Co bands. The crystal structure is closely related to it. And the electron environment around the orbitals of octahedron will be complicated due to the structural distortion, which increases the electron density of overlapped band for O and Co. Therefore, intense charge transfer would be generated when Fermi level passes through the overlapped band of the cathode with distorted structure. With the occurrence of adverse charge transfer, the structural distortion in turns to become more obvious, resulting in further band overlap and charge transfer.

Based on the results, a unified redox mechanism is proposed (Figure 6). The difference in band structure will have an important effect on the redox mechanism. The spin state of Co influences the band structure. For LS-LCO, the low spin of Co causes a high overlap between t_{2g} and O 2p. With charge, electrons are firstly extracted from t_{2g} band, which oxidizes the low-spin Co³⁺ ($t_{2g}^6 e_g^0$) to Co⁴⁺ ($t_{2g}^5 e_g^1$). When half of the Co³⁺ cations are oxidized to Co⁴⁺, the Fermi level meets O 2p state. With further oxidation, O \rightarrow Co charge transfer is triggered, which reduces Co⁴⁺ to Co³⁺ or even Co⁰⁺ and simultaneously oxidizes O²⁻ to O₂. In this process, some CoO₆ octahedrons generate shortened O-O distance and elongated Co-O bond length, complicating the structural properties and inducing a hybrid H1-3 phase. Obvious heterogeneous lattice changes and CoO₆ distortions are thus generated, which further exacerbates band overlap and adverse charge transfer behaviors. After the charge-discharge cycle, the electronic structure could not recover to its pristine state due to the irreversible reactions and unrecovered structural changes. Moreover, the OAR and O-O shortening exhibit a slow kinetics, which reduces the reacting rate of the whole reactions.

While for HS-LCO, high spin Co induces a reduced overlap

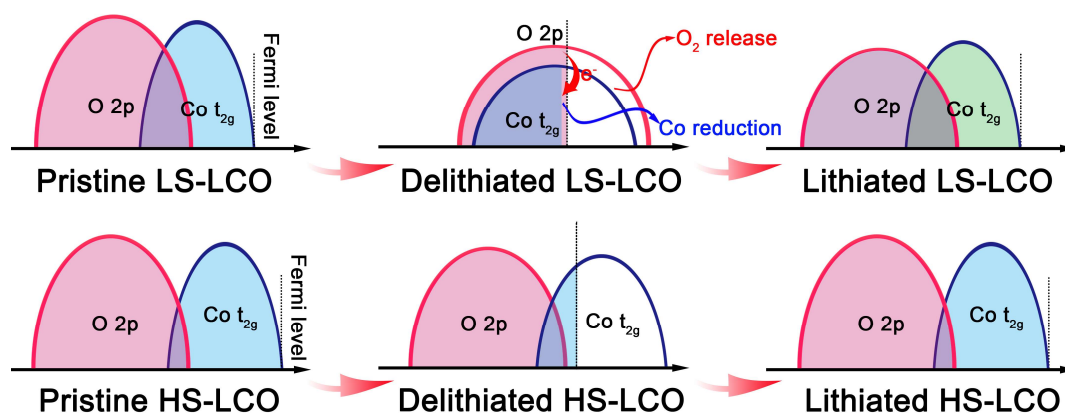


Figure 6. Sketch for illustrating the redox mechanism for LS-LCO and HS-LCO.

between t_{2g} and O 2p. And the lattice stress field generated by nanoribboned network structure restrains the structural changes upon delithiating. These functions postpone the approaching of Fermi level to O 2p band at high voltages and fundamentally addresses the unfavored O \rightarrow Co charge transfer. The over-oxidation of lattice O and over-reduction of Co are thus fundamentally eliminated. A deepened Co redox combined with little O redox is exhibited. Because of its stable chemical reactions, HS-LCO has higher reversible capacity and stability. Moreover, the simplified charge-discharge mechanism of HS-LCO inhibits the shortening of O-O distance and the elongation of Co-O at high voltages, which further helps the delithiated HS-LCO to maintain the O3 phase. This gives HS-LCO a better structural reversibility. Moreover, the inhibition of phase transition restrains the structural distortions, which fundamentally alleviates the band overlap and the resulted unfavored O \rightarrow Co charge transfer. Therefore, after charge and discharge, the band structure of HS-LCO can recover to the pristine state. And because of the introduction of high spin Co and the suppression of lattice oxygen reaction, the kinetics of the whole reactions is largely improved. Moreover, the morphological features across a wide range of length scales also have a very significant role to play. A small particle size contributes to the fast Li transport dynamics.⁴⁵ And in addition, particle size influences the spin state as well.²⁸

In order to explore the role of added elements, we did a preliminary investigation. Based on the amounts of added elements for HS-LCO, the samples added with only Ni, Mn (labeled as LCO-NiMn) and with only Zr (labeled as LCO-Zr) were synthesized, respectively. The SEM images, XRD plots, and electrochemical properties are shown in Figure S35. It could be seen that the Ni/Mn element divides the LCO particles. Obvious lattice mismatch stress is expressed in LCO-Zr but not in LCO-NiMn, evidenced by the relative 003 peak intensity and the charge-discharge curves. From the electrochemical results, it concludes that LCO-Zr cannot maintain the lattice mismatch stress stably. These results demonstrate that Ni/Mn, Zr elements should be together to maintain the interfacial lattice mismatch stress.

The Zr in HS-LCO has been shown to be unevenly distributed by Figure S10. This is related to the grain fusion characteristic of HS-LCO. A certain degree of the atomic mismatch is formed at the grain-fused interface, which enhances the lattice energy and the solubility of Zr element near the fused region.

And the atomic mismatches and defects at the lattice interface account for high spin state of Co cations. The maintenance of

the atomic mismatches and defects is the key for the reversible redox of the high spin Co cations. Zr has a positive effect on improving structural stability. Moreover, Zr⁴⁺ introduction favors the formation of Co²⁺, which deepens the structural distortions and favors the high spin state. Therefore, the enrichment of Zr at the fusion interface is beneficial to generate and stabilize the high spin state of Co cations in HS-LCO. This plays an important role in the reversible redox of high spin Co. It is concluded that to construct stable lattice stress field, the additive needs elements with good compatibility with the host, as well as other elements with large ionic sizes to induce lattice differences.

CONCLUSIONS

In summary, an atomically engineered high spin LCO is synthesized through constructing a defective nanoribboned network. Orbital reconstruction is induced to change Co from low spin state ($t_{2g}^6 e_g^0$) to high spin state ($t_{2g}^5 e_g^1$). A tuned redox mechanism with almost only Co redox is demonstrated. Firstly, the high spin Co network eliminates the adverse phase transition of O3 \rightarrow H1-3, delays the exceeding of O 2p band over the Fermi level and the resulted excessive O \rightarrow Co charge transfer at high voltages. It intrinsically promotes the Co redox and restrains the O redox, fundamentally addressing the issues of O₂ release and coupled detrimental Co reduction. Moreover, the chemo-mechanical heterogeneity caused by different kinetics of Co/O redox centers and the inferior rate performance limited by slow O redox kinetics are simultaneously improved owing to the suppression of slow OAR and the excitation of fast Co redox. And because of the high electron energy occupied state and the simplified electronic structure evolution, the high spin state enhances the activity and reversibility of Co redox in LCO. These fundamentally improves the discharge capacity, cycling stability, and rate capability of the 4.6V LCO. HS-LCO delivers high capacities of about 216 mAh g⁻¹ (@1C), 195 mAh g⁻¹ (@5C) and superior cycling retentions of 86.9% (@500 cycles@5C). The stabilized high-capacity delivered by HS-LCO promises to build next generation Li-ions batteries. The proposed insights on the importance of spin state modulation in tuning cationic/anionic redox chemistry are applicable to other O redox cathodes.

ASSOCIATED CONTENT

Supporting Information

The Supporting Information is available free of charge on the ACS Publications website.

XRD patterns of precursors, cathodes; SEM and AC-STEM images for cathodes; XPS for cathodes; EPR and NMR of cathodes; GITT and EIS for cathodes; cycling performances of cathodes; Rietveld refinements for the in situ XRD plots; ex situ Raman spectra for electrodes; EXAFS data for electrodes; Co-L3 edge XAS spectra for electrodes; O K-edge RIXS mappings of the electrodes; Cell parameters derived from XRD/ND Rietveld refinement.

AUTHOR INFORMATION

Corresponding Author

Xiangfeng Liu – Center of Materials Science and Optoelectronics Engineering, College of Materials Science and Optoelectronic Technology, University of Chinese Academy of Sciences, Beijing 100049, P. R. China; CAS Center for Excellence in Topological Quantum Computation, University of Chinese Academy of Sciences, Beijing 100190, P. R. China; orcid.org/0000-0001-9633-7721; Email: liuxf@ucas.ac.cn

Authors

Jicheng Zhang – Center of Materials Science and Optoelectronics Engineering, College of Materials Science and Optoelectronic Technology, University of Chinese Academy of Sciences, Beijing 100049, P. R. China

Deniz Wong – Dynamik und Transport in Quantenmaterialien, Helmholtz-Zentrum Berlin für Materialien und Energie, Hahn-Meitner-Platz 1, D-14109 Berlin, Germany

Qinghua Zhang – Beijing National Laboratory for Condensed Matter Physics, Institute of Physics, Chinese Academy of Science, Beijing 100190, P. R. China

Nian Zhang – Shanghai Institute of Microsystem and Information Technology, Chinese Academy of Sciences, Shanghai 200050, P. R. China

Christian Schulz – Dynamik und Transport in Quantenmaterialien, Helmholtz-Zentrum Berlin für Materialien und Energie, Hahn-Meitner-Platz 1, D-14109 Berlin, Germany

Maciej Bartkowiak – Dynamik und Transport in Quantenmaterialien, Helmholtz-Zentrum Berlin für Materialien und Energie, Hahn-Meitner-Platz 1, D-14109 Berlin, Germany

Ke An – Neutron Scattering Division, Oak Ridge National Laboratory, Oak Ridge, Tennessee 37830, United States

Lin Gu – Beijing National Laboratory for Condensed Matter Physics, Institute of Physics, Chinese Academy of Science, Beijing 100190, P. R. China

Zhongbo Hu – Center of Materials Science and Optoelectronics Engineering, College of Materials Science and Optoelectronic Technology, University of Chinese Academy of Sciences, Beijing 100049, P. R. China

Notes

The authors declare no competing financial interest

ACKNOWLEDGMENT

This work was supported by the National Natural Science Foundation of China (Grant No. 22005302, 11975238 and 11575192), the International Partnership Program (Grant No. 211211KYSB20170060 and 211211KYSB20180020), the Scientific Instrument Developing Project (Grant No. ZDKYYQ20170001), the Strategic Priority Research Program (Grant No. XDB28000000) of the Chinese Academy of Sciences, and the Natural Science Foundation of Beijing (Grant No. 2182082). This work was also supported by the China Postdoctoral Science Foundation (2020M680648) and the Fundamental Research Funds for the Central Universities. The authors thank the staff from BL14W1 beamline, 02B02 beamline of SSRF for their help and support. The authors also thank the staff from PEAXIS beamline of synchrotron BESSY II at Helmholtz-Zentrum Berlin (HZB).

REFERENCES

- (1) Wang, L.; Chen, B.; Ma, J.; Cui, G.; Chen, L. Reviving lithium cobalt oxide-based lithium secondary batteries-toward a higher energy density. *Chem. Soc. Rev.* **2018**, *47*, 6505–6602.
- (2) Montoro, L. A.; Abbate, M.; Rosolen, J. M. Changes in the electronic structure of chemically deintercalated LiCoO₂. *Electrochem. Solid-State Lett.* **2000**, *3*, 410–412.
- (3) Chen, J.; Chen, H.; Zhang, S.; Dai, A.; Li, T.; Mei, Y.; Ni, L.; Gao, X.; Deng, W.; Yu, L.; Zou, G.; Hou, H.; Dahbi, M.; Xu, W.; Wen, J.; Alami, J.; Liu, T.; Amine, K.; Ji, X. Structure/interface coupling effect for high-voltage LiCoO₂ cathodes. *Adv. Mater.* **2022**, *34*, 2204845.
- (4) Wang, Y.; Zhang, Q.; Xue, Z.-C.; Yang, L.; Wang, J.; Meng, F.; Li, Q.; Pan, H.; Zhang, J.-N.; Jiang, Z.; Yang, W.; Yu, X.; Gu, L.; Li, H. An in situ formed surface coating layer enabling LiCoO₂ with stable 4.6 V high-voltage cycle performances. *Adv. Energy Mater.* **2020**, *10*, 2001413.
- (5) Li, J.; Lin, C.; Weng, M.; Qiu, Y.; Chen, P.; Yang, K.; Huang, W.; Hong, Y.; Li, J.; Zhang, M.; Dong, C.; Zhao, W.; Xu, Z.; Wang, X.; Xu, K.; Sun, J.; Pan, F. Structural origin of the high-voltage instability of lithium cobalt oxide. *Nat. Nanotechnol.* **2021**, *16*, 599–605.
- (6) Li, S.; Li, K.; Zheng, J.; Zhang, Q.; Wei, B.; Lu, X. Structural distortion-induced charge gradient distribution of Co ions in delithiated LiCoO₂ cathode. *J. Phys. Chem. Lett.* **2019**, *10*, 7537–7546.
- (7) Sun, G.; Yu, F.-D.; Lu, M.; Zhu, Q.; Jiang, Y.; Mao, Y.; McLeod, J. A.; Maley, J.; Wang, J.; Zhou, J.; Wang, Z. Surface chemical heterogeneous distribution in over-lithiated Li_{1+x}CoO₂ electrodes. *Nat. Commun.* **2022**, *13*, 6464.
- (8) Cai, M.; Dong, Y.; Xie, M.; Dong, W.; Dong, C.; Dai, P.; Zhang, H.; Wang, X.; Sun, X.; Zhang, S.; Yoon, M.; Xu, H.; Ge, Y.; Li, J.; Huang, F. Stalling oxygen evolution in high-voltage cathodes by lanthanization. *Nat. Energy* **2023**, *8*, 159–168.
- (9) Wen, M.; Kong, W.; Zhang, J.; Zhang, Q.; Yin, W.; Zhang, N.; Chai, K.; Yu, Y.; Chen, H.; Liu, X. Tuning Co/O redox chemistry via Fermi level regulation for stable high-voltage LiCoO₂. *ACS Energy Lett.* **2022**, *7*, 4185–4189.
- (10) Xu, Y.; Hu, E.; Zhang, K.; Wang, X.; Borzenets, V.; Sun, Z.; Pianetta, P.; Yu, X.; Liu, Y.; Yang, X.-Q.; Li, H. In situ visualization of state-of-charge heterogeneity within a LiCoO₂ particle that evolves upon cycling at different rates. *ACS Energy Lett.* **2017**, *2*, 1240–1245.
- (11) Sharifi-Asl, S.; Soto, F. A.; Foroozan, T.; Asadi, M.; Yuan, Y.; Deivanayagam, R.; Rojaee, R.; Song, B.; Bi, X.; Amine, K.; Lu, J.; Salehi-khojin, A.; Balbuena, P. B.; Shabbazian-Yassar, R. Anti-oxygen leaking LiCoO₂. *Adv. Funct. Mater.* **2019**, *29*, 1901110.
- (12) Zhang, J.-N.; Li, Q.; Ouyang, C.; Yu, X.; Ge, M.; Huang, X.; Hu, E.; Ma, C.; Li, S.; Xiao, R.; Yang, W.; Chu, Y.; Liu, Y.; Yu,

- H.; Yang, X.-Q.; Huang, X.; Chen, L.; Li, H. Trace doping of multiple elements enables stable battery cycling of LiCoO₂ at 4.6 V. *Nat. Energy* **2019**, *4*, 594–603.
- (13) Qian, J.; Liu, L.; Yang, J.; Li, S.; Wang, X.; Zhuang, H. L.; Lu, Y. Electrochemical surface passivation of LiCoO₂ particles at ultrahigh voltage and its applications in lithium-based batteries. *Nat. Commun.* **2018**, *9*, 4918.
- (14) Huang, Y.; Zhu, Y.; Fu, H.; Ou, M.; Hu, C.; Yu, S.; Hu, Z.; Chen, C.-T.; Jiang, G.; Gu, H.; Lin, H.; Luo, W.; Huang, Y. Mg-pillared LiCoO₂: towards stable cycling at 4.6 V. *Angew. Chem. Int. Ed.* **2021**, *133*, 4732–4738.
- (15) Kong, W.; Zhang, J.; Wong, D.; Yang, W.; Yang, J.; Schulz, C.; Liu, X. Tailoring Co3d and O2p band centers to inhibit oxygen escape for stable 4.6 V LiCoO₂ cathodes. *Angew. Chem. Int. Ed.* **2021**, *60*, 27102–27112.
- (16) Liu, Q.; Su, X.; Lei, D.; Qin, Y.; Wen, J.; Guo, F.; Wu, Y. A.; Rong, Y.; Kou, R.; Xiao, X.; Aguesse, F.; Bareño, J.; Ren, Y.; Lu, W.; Li, Y. Approaching the capacity limit of lithium cobalt oxide in lithium ion batteries via lanthanum and aluminium doping. *Nat. Energy* **2018**, *3*, 936–943.
- (17) Tan, X.; Zhao, T.; Song, L.; Mao, D.; Zhang, Y.; Fan, Z.; Wang, H.; Chu, W. Simultaneous near-surface trace doping and surface modifications by gas–solid reactions during one-pot synthesis enable stable high-voltage performance of LiCoO₂. *Adv. Energy Mater.* **2022**, *12*, 2200008.
- (18) Zhu, Z.; Yu, D.; Shi, Z.; Gao, R.; Xiao, X.; Waluyo, I.; Ge, M.; Dong, Y.; Xue, W.; Xu, G.; Lee, W.-K.; Hunt, A.; Li, J. Gradient-morph LiCoO₂ single crystals with stabilized energy density above 3400 Wh L⁻¹. *Energy Environ. Sci.* **2020**, *13*, 1865–1878.
- (19) Fan, T.; Kai, W.; Harika, V. K.; Liu, C.; Nimkar, A.; Leifer, N.; Maiti, S.; Grinblat, J.; Tsubery, M. N.; Liu, X.; Wang, M.; Xu, L.; Lu, Y.; Min, Y.; Shpigel, N.; Aurbach, D. Operating highly stable LiCoO₂ cathodes up to 4.6 V by using an effective integration of surface engineering and electrolyte solutions selection. *Adv. Funct. Mater.* **2022**, *32*, 2204972.
- (20) Zhang, J.; Wang, P.-F.; Bai, P.; Wan, H.; Liu, S.; Hou, S.; Pu, X.; Xia, J.; Zhang, W.; Wang, Z.; Nan, B.; Zhang, X.; Xu, J.; Wang, C. Interfacial design for a 4.6 V high-voltage single-crystalline LiCoO₂ cathode. *Adv. Mater.* **2022**, *34*, 2108353.
- (21) Qin, N.; Gan, Q.; Zhuang, Z.; Wang, Y.; Li, Y.; Li, Z.; Hussain, I.; Zeng, C.; Liu, G.; Bai, Y.; Zhang, K.; Lu, Z. Hierarchical doping engineering with active/inert dual elements stabilizes LiCoO₂ to 4.6 V. *Adv. Energy Mater.* **2022**, *12*, 2201549.
- (22) Rouxel, J. Some solid state chemistry with holes: anion–cation redox competition in solids. *Curr. Sci.* **1997**, *73*, 31–39.
- (23) Liu, T.; Liu, J.; Li, L.; Yu, L.; Diao, J.; Zhou, T.; Li, S.; Dai, A.; Zhao, W.; Xu, S.; Ren, Y.; Wang, L.; Wu, T.; Qi, R.; Xiao, Y.; Zheng, J.; Cha, W.; Harder, R.; Robinson, I.; Wen, J.; Lu, J.; Pan, F.; Amine, K. Origin of structural degradation in Li-rich layered oxide cathode. *Nature* **2022**, *606*, 305–312.
- (24) Hu, E.; Li, Q.; Wang, X.; Meng, F.; Liu, J.; Zhang, J.-N.; Page, K.; Xu, W.; Gu, L.; Xiao, R.; Li, H.; Huang, X.; Chen, L.; Yang, W.; Yu, X.; Yang, X.-Q. Oxygen-redox reactions in LiCoO₂ cathode without O–O bonding during charge-discharge. *Joule* **2021**, *5*, 720–736.
- (25) Niemöllera, A.; Jakesa, P.; Eichel, R.-A.; Granwehr, J. In operando EPR investigation of redox mechanisms in LiCoO₂. *Chem. Phys. Lett.* **2019**, *716*, 231–236.
- (26) Hua, W.; Yang, X.; Casati, N. P. M.; Liu, L.; Wang, S.; Baran, V.; Knapp, M.; Ehrenberg, H.; Indris, S. Probing thermally-induced structural evolution during the synthesis of layered Li-, Na-, or K-containing 3d transition-metal oxides. *eScience* **2022**, *2*, 183–191.
- (27) Sim, S.-J.; Lee, S.-H.; Jin, B.-S.; Kim, H.-S. Effects of lithium tungsten oxide coating on LiNi_{0.90}Co_{0.05}Mn_{0.05}O₂ cathode material for lithium-ion batteries. *J. Power Sources* **2021**, *481*, 229037.
- (28) Qian, D.; Hinuma, Y.; Chen, H.; Du, L.-S.; Carroll, K. J.; Ceder, G.; Grey, C. P.; Meng, Y. S. Electronic spin transition in nanosize stoichiometric lithium cobalt oxide. *J. Am. Chem. Soc.* **2012**, *134*, 6096–6099.
- (29) Chen, S.; Zhang, Q.; Li, X.; Zhao, J.; Lin, S.; Jin, Q.; Hong, H.; Huon, A.; Charlton, T.; Li, Q.; Yan, W.; Wang, J.; Ge, C.; Wang, C.; Wang, B.; Fitzsimmons, M. R.; Guo, H.; Gu, L.; Yin, W.; Jin, K.-j.; Guo, E. J. Atomically engineered cobaltite layers for robust ferromagnetism. *Sci. Adv.* **2022**, *8*, eabq3981.
- (30) Liu, S.; Fossati, A.; Serrano, D.; Tallaire, A.; Ferrier, A.; Goldner, P. Defect engineering for quantum grade rare-earth nanocrystals. *ACS Nano* **2020**, *14*, 9953–9962.
- (31) Levasseur, S.; Ménétrier, M.; Delmas, C. On the dual effect of Mg doping in LiCoO₂ and Li_{1+x}CoO₂: structural, electronic properties, and ⁷Li MAS NMR studies. *Chem. Mater.* **2002**, *14*, 3584–3590.
- (32) Zhang, J.; Zhang, Q.; Wong, D.; Zhang, N.; Ren, G.; Gu, L.; Schulz, C.; He, L.; Yu, Y.; Liu, X. Addressing voltage decay in Li-rich cathodes by broadening the gap between metallic and anionic bands. *Nat. Commun.* **2021**, *12*, 3071.
- (33) Mizokawa, T.; Wakisaka, Y.; Sudayama, T.; Iwai, C.; Miyoshi, K.; Takeuchi, J.; Wadati, H.; Hawthorn, D. G.; Regier, T. Z.; Sawatzky, G. A. Role of oxygen holes in Li_xCoO₂ revealed by soft X-ray spectroscopy. *Phys. Rev. Lett.* **2013**, *111*, 056404.
- (34) K. S. Kim, X-ray-photoelectron spectroscopic studies of the electronic structure of CoO. *Phys. Rev. B* **1975**, *11*, 2177–2185.
- (35) Li, S.; Lee, S.-J.; Wang, X.; Yang, W.; Huang, H.; Swetz, D. S.; Doriese, W. B.; O’Neil, G. C.; Ullom, J. N.; Titus, C. J.; Irwin, K. D.; Lee, H.-K.; Nordlund, D.; Pianetta, P.; Yu, C.; Qiu, J.; Yu, X.; Yang, X.-Q.; Hu, E.; Lee, J.-S.; Liu, Y. Surface-to-bulk redox coupling through thermally driven Li redistribution in Li- and Mn-rich layered. *J. Am. Chem. Soc.* **2019**, *141*, 12079–12086.
- (36) Luo, K.; Roberts, M. R.; Hao, R.; Guerrini, N.; Pickup, D. M.; Liu, Y.-S.; Edström, K.; Guo, J.; Chadwick, A. V.; Duda, L. C.; Bruce, P. G. Charge-compensation in 3d-transition-metal-oxide intercalation cathodes through the generation of localized electron holes on oxygen. *Nat. Chem.* **2016**, *8*, 684–691.
- (37) House, R. A.; Maitra, U.; Pérez-Osorio, M. A.; Lozano, J. G.; Jin, L.; Somerville, J. W.; Duda, L. C.; Nag, A.; Walters, A.; Zhou, K.-J.; Roberts, M. R.; Bruce, P. G. Superstructure control of first-cycle voltage hysteresis in oxygen-redox cathodes. *Nature* **2020**, *577*, 502–508.
- (38) Duffiet, M.; Blangero, M.; Cabelguen, P.-E.; Delmas, C.; Carlier, D. Influence of the initial Li/Co ratio in LiCoO₂ on the high-voltage phase-transitions mechanisms. *J. Phys. Chem. Lett.* **2018**, *9*, 5334–5338.
- (39) Liu, J.; Wang, J.; Ni, Y.; Liu, J.; Zhang, Y.; Lu, Y.; Yan, Z.; Zhang, K.; Zhao, Q.; Cheng, F.; Chen, J. Tuning interphase chemistry to stabilize high-voltage LiCoO₂ cathode material via spinel coating. *Angew. Chem. Int. Ed.* **2022**, *61*, e202207000.
- (40) Zhu, Z.; Wang, H.; Li, Y.; Gao, R.; Xiao, X.; Yu, Q.; Wang, C.; Waluyo, I.; Ding, J.; Hunt, A.; Li, J. A surface Se-substituted LiCo[O_{2-δ}Se_δ] cathode with ultrastable high-voltage cycling in pouch full-cells. *Adv. Mater.* **2020**, *32*, 2005182.
- (41) Yan, Y.; Wang, S.; Fu, A.; Zhang, H.; Chen, J.; Zheng, Q.; Zhang, B.; Zhou, S.; Yan, H.; Wang, C.-W.; Tang, Y.; Luo, H.; Mao, B.-W.; Zheng, J.; Wang, X.; Qiao, Y.; Yang, Y.; Sun, S.-G. Tailoring electrolyte dehydrogenation with trace additives: stabilizing the LiCoO₂ cathode beyond 4.6 V. *ACS Energy Lett.* **2022**, *7*, 2677–2684.
- (42) Julien, C. Local cationic environment in lithium nickel–cobalt oxides used as cathode materials for lithium batteries. *Solid State Ion.* **2000**, *136–137*, 887–896.
- (43) Huang, H.; Li, Z.; Gu, S.; Bian, J.; Li, Y.; Chen, J.; Liao, K.; Gan, Q.; Wang, Y.; Wu, S.; Wang, Z.; Luo, W.; Hao, R.; Wang, Z.; Wang, G.; Lu, Z. Dextran sulfate lithium as versatile binder to stabilize high-voltage LiCoO₂ to 4.6 V. *Adv. Energy Mater.* **2021**, *11*, 2101864.

(44) Assat, G.; Tarascon, J.-M. Fundamental understanding and practical challenges of anionic redox activity in Li-ion batteries. *Nat. Energy* **2018**, *3*, 373–386.

(45) Li, J.; Sharma, N.; Jiang, Z.; Yang, Y.; Monaco, F.; Xu, Z.; Hou, D.; Ratner, D.; Pianetta, P.; Cloetens, P.; Lin, F.; Zhao, K.;

Liu, Y.; Dynamics of particle network in composite battery cathodes. *Science* **2022**, *376*, 517–521.

The intrinsic inferior thermodynamics and kinetics issues of O anion redox (OAR) inherently deteriorate the high-voltage LiCoO₂. Herein, an atomically engineered high spin LiCoO₂ demonstrates a tuned redox mechanism with almost only Co redox, which fundamentally addresses the unfavorable issues. The redox modulation originates from the restriction of Fermi level to *t*_{2g} band by the high spin Co framework.

